An Implicit Algebraic Turbulence Closure Scheme for Atmospheric Boundary Layer Simulation

XIAOMING SHI

Division of Environment and Sustainability, and Department of Civil and Environmental Engineering, Hong Kong University of Science and Technology, Hong Kong, China

RICA MAE ENRIQUEZ[a] AND ROBERT L. STREET

Department of Civil and Environmental Engineering, Stanford University, Stanford, California

GEORGE H. BRYAN

National Center for Atmospheric Research, Boulder, Colorado

FOTINI KATOPODES CHOW

Department of Civil and Environmental Engineering, University of California, Berkeley, Berkeley, California

(Manuscript received 22 December 2018, in final form 11 August 2019)

ABSTRACT

Turbulence parameterization plays a critical role in the simulation of many weather regimes. For challenging cases such as the stratocumulus-capped boundary layer (SCBL), traditional schemes can produce unrealistic results even when a fine large-eddy-simulation (LES) resolution is used. Here we present an implicit generalized linear algebraic subfilter-scale model (iGLASS) to better represent unresolved turbulence in the simulation of the atmospheric boundary layer, at both standard LES and so-called *terra incognita* (TI) resolutions. The latter refers to a range of model resolutions where turbulent eddies are only partially resolved, and therefore the simulated processes are sensitive to the representation of unresolved turbulence. iGLASS is based on the truncated conservation equations of subfilter-scale (SFS) fluxes, but it integrates the full equations of the SFS turbulence kinetic energy and potential energy to retain ''memory'' of the SFS turbulence. Our evaluations suggest iGLASS can perform significantly better than traditional eddy-diffusivity models and exhibit skills comparable to the dynamic reconstruction model (DRM). For a neutral boundary layer case run at LES resolution, the simulation using iGLASS exhibits a wind profile that reasonably matches the similarity-theory solution. For an SCBL case with 5-m vertical resolution, iGLASS maintains more realistic cloud water profiles and boundary layer structure than traditional schemes. The SCBL case is also tested at TI resolution, and iGLASS also exhibits superior performance. iGLASS permits significant backscatter, whereas traditional models allow forward scatter (diffusion) only. As a physics-based approach, iGLASS appears to be a viable alternative for turbulence parameterization.

1. Introduction

Kilometer-scale resolution has become possible in regional numerical weather prediction and climate simulation in recent years (Hagelin et al. 2017; Prein et al. 2015). While the refined numerical mesh allows more detailed representation of the weather and climate, it also moves atmospheric modeling into terra incognita (TI), where the most energetic eddies in turbulent processes are only partially resolved (Wyngaard 2004).

The parameterization of turbulence in TI is challenging, because traditional closure schemes assume the energy-containing eddies are either mostly resolved [in large-eddy simulation (LES)] or unresolved (in mesoscale and global models), and therefore each of their key

[a] Current affiliation: Geosyntec Consultants, Inc., Boca Raton, Florida.

Corresponding author: Xiaoming Shi, shixm@ust.hk

DOI: 10.1175/JAS-D-18-0375.1

assumptions are violated in TI. For example, the grid spacing of LES is assumed to be in the inertial subrange, thus traditional LES-type turbulence schemes are entirely dissipative/diffusive, that is, their net effect is to transfer kinetic energy and scalar turbulence from resolved scales to unresolved scales. However, backscatter, the transfer of kinetic energy and scalar variance from unresolved scales to resolved scales, is important when simulating clouds and convection in TI. Accordingly, failing to represent backscatter can significantly lower the fidelity of the simulations by misrepresenting turbulent transport and clouds (Verrelle et al. 2017; Shi et al. 2019, 2018). Another example is that traditional turbulence schemes in mesoscale and global models, including planetary boundary layer (PBL) schemes and cumulus convection parameterizations, assume horizontal homogeneity of turbulence and thus produce mixing in the vertical direction only. However, at kilometer-scale resolutions, horizontal mixing has been shown to be important for the simulation of many processes, such as the convective boundary layer (Ching et al. 2014), organized convection (Tompkins and Semie 2017), and tropical cyclones (Bryan and Rotunno 2009).

One strategy to develop better turbulence closures for TI is to start with the conservation equations of subfilter-scale (SFS) fluxes and derive some appropriately truncated versions of them (Wyngaard 2004; Hatlee and Wyngaard 2007; Ramachandran and Wyngaard 2011). The idea of using SFS conservation equations to compute turbulent mixing can be traced back to the early work of Deardorff in the 1970s (Deardorff 1974), but because of the prohibitive computational cost at the time, simpler eddy-diffusivity closures became widely adopted instead. The well-known hierarchy of turbulence closures developed by Mellor and Yamada (1982) includes both the full conservation equations (their level-4 model) and truncated versions (level-3, -2.5, and -2 models). With the assumption of horizontal homogeneity and other simplifications, current Mellor–Yamada-type PBL schemes are essentially eddy-diffusivity-based models, though countergradient fluxes can be enabled by including a gradient adjustment term (e.g., Nakanishi and Niino 2009).

The first attempt to create a better turbulence closure for TI by using truncated conservation equations was by Wyngaard (2004), who retained the complete set of production terms and argued a tensorial eddy diffusivity is needed for the simplest model consistent with the conservation equations. Hatlee and Wyngaard (2007) and Ramachandran and Wyngaard (2011) evaluated a turbulence closure with prognostic SFS-flux equations that additionally include advection and buoyancy production terms, and they found it exhibits superior performance than a simple eddy-diffusivity closure. In their simulations of a dry convective boundary layer, Ramachandran and Wyngaard (2011) found that the prognostic SFS model increases computational cost by a factor of about 2, which could become even larger if moist processes were included.

To reduce the computational cost of conservation-equation-based closures, algebraic turbulence models were developed by Rodi (1976) and Findikakis and Street (1979), who neglected the material derivatives in the SFS conservation equations and solved the resulting algebraic equations to obtain SFS fluxes. Building upon those early works, Enriquez (2013) developed an implicit generalized linear algebraic subfilter-scale model (iGLASS) and applied it to LES of the atmospheric boundary layer (ABL). Differing from explicit algebraic models (e.g., Marstorp et al. 2009; Lazeroms et al. 2016), which seek explicit expression of SFS fluxes with approximation, iGLASS solves the algebraic equations by inverting matrices. Its solution is intrinsically three-dimensional, anisotropic, and allows backscatter. iGLASS has shown promising performance, improving over traditional LES closures, in simulations of the dry ABL under different stability conditions (Enriquez 2013; Enriquez et al. 2010, 2012; Enriquez and Street 2014).

Here we apply iGLASS to the simulations of both dry and moist ABL flows and evaluate its performance in the terra incognita. The governing equations of iGLASS are modified to make them appropriate for simulating clouds with Cloud Model 1 (CM1; section 2). Important changes include the addition of 1) a prognostic equation for turbulence potential energy (the SFS variance of potential temperature) and 2) a procedure to detect and treat ''singular'' solutions. The first change is implemented because of the critical role buoyancy flux plays in driving the turbulent flows of cloudy boundary layers. The second change is needed because when the quasi-equilibrium (QE) assumption of algebraic models is violated, the resulting erroneous fluxes can cause numerical instabilities in the host model. Both of these changes are not necessary for simple dry ABL flows, but they become critical when clouds are involved due to the increased complexity of the flow regarding energy generation and conversion. As shown below, the performance of this extended version of iGLASS is not only better than traditional eddy-diffusivity models, but also comparable to the dynamic reconstruction turbulence closure model (DRM) (Chow et al. 2005; Shi et al. 2018) at both LES and TI resolutions. iGLASS has similar computational cost to DRM.

Because iGLASS has been extended in a new code, CM1, we first evaluate iGLASS in a dry neutral boundary layer (NBL) case (section 3). Then we move on to testing and analyzing the performance of iGLASS in the challenging case of the stratocumulus-capped boundary layer (SCBL) at both LES and TI resolutions (section 4).

2. Turbulence closure schemes

a. LES governing equations

The LES code used in this study is CM1 (release 18), which solves the nonhydrostatic, compressible equations of the moist atmosphere (Bryan and Fritsch 2002). Because the governing equations for CM1 have some notable differences with the equations for some other models, the SFS conservation equations for the iGLASS in this study are somewhat different from those in previous studies. Here we briefly describe the CM1 governing equations. Detailed derivation of the CM1 equations can be found in Bryan and Fritsch (2002).

In CM1, the governing equations for the three velocity components u_i are

$$\frac{D\overline{u}_i}{Dt} = -c_p\overline{\theta}_\rho\frac{\partial\overline{\pi'}}{\partial x_i} + \delta_{i3}\overline{B} + \epsilon_{ij3}f\overline{u}_j - \frac{1}{\hat{\rho}}\frac{\partial(\hat{\rho}\tau_{ij})}{\partial x_j}, \quad (1)$$

where c_p is specific heat of dry air at constant pressure, δ_{ij} and ϵ_{ijk} are the Kronecker delta and alternating tensor, respectively, and f is the Coriolis parameter. In Eq. (1), θ_ρ is density potential temperature,

$$\theta_\rho = \theta\left(\frac{1+q_v/\varepsilon}{1+q_t}\right), \quad (2)$$

where θ is potential temperature, q_v and q_t are water vapor and total water mixing ratio, respectively, and ε is the ratio of the gas constant for dry air R_d to that for water vapor R_v. The term $\pi = (p/p_{\text{ref}})^{R_d/c_p}$ is the Exner function, where p denotes pressure and p_{ref} is a reference value. In CM1, a variable can be decomposed into a base-state part (denoted by a subscript 0) and a perturbation part (denoted by a prime), for example, $\pi = \pi_0 + \pi'$, where the base-state part is invariant in time and varies in the vertical direction only. In Eq. (1) B is buoyancy and its linearized form is used in model integration,

$$B = g\frac{\theta_\rho - \theta_{\rho 0}}{\theta_{\rho 0}} \cong g\left[\frac{\theta'}{\theta_0} + \left(\frac{1}{\varepsilon}-1\right)q_v' - (q_t - q_v)\right], \quad (3)$$

where g is the gravitational acceleration. The hat (^) and overline (¯) in Eq. (1) denote the spatial filter for density ρ and the Favre (density weighted) filter (Favre 1983; Moin et al. 1991) for the other variables in the LES. The usage of the Favre filter helps avoid having an SFS term in the mass conservation equation. θ_0 and $\theta_{\rho 0}$ are reference state profiles for simulation. The SFS stress τ_{ij} is defined as

$$\tau_{ij} = \overline{u_i u_j} - \overline{u}_i\overline{u}_j. \quad (4)$$

For potential temperature, the governing equation is

$$\frac{D\overline{\theta}}{Dt} = \overline{\dot{Q}}_\theta - \frac{1}{\hat{\rho}}\frac{\partial(\hat{\rho}\tau_{\theta j})}{\partial x_j}, \quad (5)$$

where $\dot{Q}_\theta$ is the heating/cooling tendency due to diabatic processes, such as radiation and microphysics. In Eq. (6) $\tau_{\theta j}$ denotes the SFS flux of θ,

$$\tau_{\theta j} = \overline{\theta u_j} - \overline{\theta}\overline{u}_j. \quad (6)$$

CM1 can include multiple water variables (vapor, liquid, ice, etc.), the governing equations for which can be written generically as

$$\frac{D\overline{q}}{Dt} = \overline{\dot{q}} - \frac{1}{\hat{\rho}}\frac{\partial(\hat{\rho}\tau_{qj})}{\partial x_j}, \quad (7)$$

where q represents the mixing ratio of one water variables, $\dot{q}$ is the tendency due to corresponding microphysical processes, and τ_{qj} is the SFS flux of q,

$$\tau_{qj} = \overline{qu_j} - \overline{q}\overline{u}_j. \quad (8)$$

For the simulations of stratocumulus cloud in this study, only two water variables are involved, water vapor q_v and cloud water q_c.

Last, the governing equation for π is

$$\frac{D\overline{\pi}}{Dt} = -\overline{\pi}\frac{R_d}{c_v}\frac{\partial\overline{u}_j}{\partial x_j}, \quad (9)$$

which does not have an SFS term because of the Favre filter. Here c_v is the specific heat of dry air at constant volume.

The energy- and mass-conserving equations of Bryan and Fritsch (2002) include additional terms in Eqs. (5) and (9) to achieve better conservation. However, the simplified forms shown above are reasonable simplifications and similar equations are used in some other models, including the Weather Research and Forecasting (WRF) Model (Skamarock et al. 2008). Thus, they are adequate for deriving the conservation equations of SFS fluxes below.

b. The formulation of iGLASS

In this section, we first present the full conservation equations consistent with the governing equations of CM1, then present the truncation and parameterization needed in iGLASS. The conservation equations for the SFS stresses are

$$\begin{aligned}\frac{D\tau_{ij}}{Dt} = &-\frac{1}{\hat{\rho}}\frac{\partial}{\partial x_k}[\hat{\rho}(\overline{u_i u_j u_k} - \overline{u}_i\overline{u}_j\overline{u}_k - \overline{u}_j\tau_{ij} - \overline{u}_k\tau_{ik} - \overline{u}_i\tau_{jk})]\\ &- \left(\tau_{ik}\frac{\partial\overline{u}_j}{\partial x_k} + \tau_{jk}\frac{\partial\overline{u}_i}{\partial x_k}\right)\\ &+ (\delta_{i3}\tau_{Bj} + \delta_{j3}\tau_{Bi})\\ &- c_p\left[\left(\overline{u_i\theta_\rho\frac{\partial\pi'}{\partial x_j}} - \overline{u}_i\overline{\theta_\rho\frac{\partial\pi'}{\partial x_j}}\right) + \left(\overline{u_j\theta_\rho\frac{\partial\pi'}{\partial x_i}} - \overline{u}_j\overline{\theta_\rho\frac{\partial\pi'}{\partial x_i}}\right)\right]\\ &+ \nu\left(\overline{u_i\frac{\partial^2 u_j}{\partial x_k\partial x_k}} + \overline{u_j\frac{\partial^2 u_i}{\partial x_k\partial x_k}}\right) + f(\epsilon_{ik3}\tau_{jk} + \epsilon_{jk3}\tau_{ik}),\end{aligned} \tag{10}$$

where the terms in each line of the right side can be named as the third-order transport, production, buoyancy generation, pressure redistribution, dissipation, and Coriolis effect, respectively. On the last line of Eq. (10) ν is the (molecular) kinematic viscosity.

The SFS buoyancy flux τ_{Bj} is defined as

$$\tau_{Bj} = \overline{Bu_j} - \overline{B}\overline{u}_j, \tag{11}$$

which can be expressed as a linear combination of SFS scalar fluxes thanks to Eq. (3). For example, when there are only two water variables q_v and q_c in the simulation, the SFS buoyancy flux can be expanded as

$$\tau_{Bj} = \frac{g}{\overline{\theta}_0}\tau_{\theta j} + g\left(\frac{1}{\varepsilon} - 1\right)\tau_{q_v j} - g\tau_{q_c j}. \tag{12}$$

This expression is the key to the coupling between the equations of SFS stress and those of SFS scalar fluxes.

The conservation equation of SFS turbulence kinetic energy (TKE), $e = \tau_{ii}/2$, can be obtained from Eq. (10) contracting and dividing by 2. The result is

$$\begin{aligned}\frac{De}{Dt} = &-\frac{1}{\hat{\rho}}\frac{\partial}{\partial x_j}[\hat{\rho}(\overline{Eu_j} - \overline{E}\overline{u}_j - \overline{u}_i\tau_{ij})] - \tau_{ij}\frac{\partial\overline{u}_i}{\partial x_j} + \tau_{B3}\\ &- c_p\left(\overline{u_i\theta_\rho\frac{\partial\pi'}{\partial x_i}} - \overline{u}_i\overline{\theta_\rho\frac{\partial\pi'}{\partial x_i}}\right) + \overline{\nu u_i\frac{\partial^2 u_i}{\partial x_j\partial x_j}},\end{aligned} \tag{13}$$

where $E = u_i u_i/2$ is kinetic energy. The terms on the right side have the same meaning as those in the corresponding line of Eq. (10), except that the Coriolis effect term does not appear in the SFS TKE equation.

The conservation equation for SFS θ flux $\tau_{\theta i}$ is

$$\begin{aligned}\frac{D\tau_{\theta i}}{Dt} = &-\frac{1}{\hat{\rho}}\frac{\partial}{\partial x_j}[\hat{\rho}(\overline{u_i u_j\theta} - \overline{u}_i\overline{u}_j\overline{\theta} - \overline{u}_j\tau_{\theta i} - \overline{u}_i\tau_{\theta j} - \overline{\theta}\tau_{ij})]\\ &- \tau_{\theta j}\frac{\partial\overline{u}_i}{\partial x_j} - \tau_{ij}\frac{\partial\overline{\theta}}{\partial x_j}\\ &+ \delta_{i3}(\overline{\theta B} - \overline{\theta}\,\overline{B})\\ &- c_p\left(\overline{\theta\theta_\rho\frac{\partial\pi'}{\partial x_i}} - \overline{\theta}\overline{\theta_\rho\frac{\partial\pi'}{\partial x_i}}\right)\\ &+ \nu\left(\overline{\theta\frac{\partial^2 u_i}{\partial x_j\partial x_j}}\right) + \alpha\left(\overline{u_i\frac{\partial^2\theta}{\partial x_j\partial x_j}}\right)\\ &+ (\overline{u_i\dot{Q}_\theta} - \overline{u}_i\overline{\dot{Q}}_\theta)\\ &+ f\epsilon_{ij3}\tau_{\theta j},\end{aligned} \tag{14}$$

where the terms in each line of the right side are third-order transport, production, buoyancy generation, pressure redistribution, diffusion, diabatic forcing, and Coriolis effect, respectively; α is thermal diffusivity. The buoyancy generation term here can be expanded with the aid of Eq. (3). Taking our stratocumulus case for example again,

$$\begin{aligned}\overline{\theta B} - \overline{\theta}\,\overline{B} = &\frac{g}{\overline{\theta}_0}(\overline{\theta^2} - \overline{\theta}^2) + g\left(\frac{1}{\varepsilon} - 1\right)(\overline{\theta q_v} - \overline{\theta}\overline{q}_v)\\ &- g(\overline{\theta q_c} - \overline{\theta}\overline{q}_c).\end{aligned} \tag{15}$$

This expansion leads to the appearance of the SFS covariance of θ and water variables in the SFS conservation equations. Though these covariance terms may be useful for microphysics parameterization, in addition to being useful for turbulence modeling, they require

adding more conservation equations. Thus, these covariance terms will be neglected below in iGLASS. This simplification only compromises iGLASS's performance when liquid/solid water contents are large, such as in tropical convection. The SFS variance of potential temperature, however, is essentially SFS turbulence potential energy (with some base-state coefficients neglected) (Zilitinkevich et al. 2007; Lazeroms et al. 2016). Therefore, it is important to keep it to have a complete description of the energy cycle. Defining SFS turbulence potential energy (TPE) as $e_p = (\overline{\theta^2} - \overline{\theta}^2)/2$, the conservation equation is

$$\frac{De_p}{Dt} = -\frac{1}{\hat{\rho}}\frac{\partial}{\partial x_j}[\hat{\rho}(\overline{E_p u_j} - \overline{E}_p\overline{u}_j - \overline{\theta}\tau_{\theta j})] - \tau_{\theta j}\frac{\partial\overline{\theta}}{\partial x_j} + (\overline{\theta\dot{Q}_\theta} - \overline{\theta}\dot{\overline{Q}}_\theta) + \alpha\overline{\theta\frac{\partial^2\theta}{\partial x_j\partial x_j}}, \tag{16}$$

where the terms on the right side are third-order transport, production, diabatic forcing, and diffusion, respectively, and $E_p = \theta^2/2$. It should be noted that e_p is only (proportional to) the SFS turbulence potential energy for a dry atmosphere. The total potential energy for a moist atmosphere includes the effect of moisture and cloud water/ice, as indicated by Eqs. (3) and (15). Defining an SFS *moist* potential energy term is possible by using the linear relationship between buoyancy and other variables (e.g., Ďurán et al. 2018), but for brevity, and because the current article focuses only on relatively small liquid water contents, we choose to use e_p only here and defer a more complete study on moist processes in iGLASS to future work.

The conservation equation of a water variable can be generically written as

$$\begin{aligned}\frac{D\tau_{qi}}{Dt} = &-\frac{1}{\hat{\rho}}\frac{\partial}{\partial x_j}[\hat{\rho}(\overline{u_i u_j q} - \overline{u}_i\overline{u}_j\overline{q} - \overline{u}_i\tau_{qj} - \overline{u}_j\tau_{qi} - \overline{q}\tau_{ij})]\\ &- \tau_{qj}\frac{\partial\overline{u}_i}{\partial x_j} - \tau_{ij}\frac{\partial\overline{q}}{\partial x_j}\\ &+ \delta_{i3}(\overline{qB} - \overline{q}\,\overline{B})\\ &- c_p\left(\overline{q\theta_\rho\frac{\partial\pi'}{\partial x_i}} - \overline{q}\,\overline{\theta_\rho\frac{\partial\pi'}{\partial x_i}}\right)\\ &+ (\overline{u_i\dot{q}} - \overline{u}_i\dot{\overline{q}})\\ &+ \nu\left(\overline{q\frac{\partial^2 u_i}{\partial x_j\partial x_j}}\right) + \alpha_q\left(\overline{u_i\frac{\partial^2 q}{\partial x_j\partial x_j}}\right)\\ &+ f\epsilon_{ij3}\tau_{qj},\end{aligned} \tag{17}$$

where the terms in each line of the right side are third-order transport, production, buoyancy generation, pressure redistribution, microphysical forcing, diffusion, and Coriolis effect, respectively, and α_p is the diffusivity of q. Again, the buoyancy generation term here can be expanded into a linear combination of the SFS covariance of θ and the water variable and that of different water variables. However, the conservation equations for those terms are not included below in iGLASS to avoid the additional computational cost.

Equations (10)–(17) form the basis of iGLASS. If we denote the number of governing equations in CM1 as $5 + n$, where n is the number of water variables, the number of conservation equations for SFS fluxes is $9 + 3n$. Integrating all of these $9 + 3n$ equations would be computationally very expensive [cf. Ramachandran and Wyngaard (2011)]. In iGLASS, we assume SFS stresses and fluxes are in QE state, so that we can neglect the material derivative, that is, the left side of Eqs. (10), (14), and (17). This QE assumption can be justified based on the fact that changes in the resolved flow are usually small in one time step, as required by numerical stability. We neglect the terms for third-order transport for convenience. Admittedly, one could use some kind of closure to parameterize the third-order term, but that requires further investigation to compare different closure approaches. The Coriolis effect in these equations is neglected too, as SFS scales are sufficiently small. The dissipation term in Eq. (10) is parameterized and kept for τ_{11}, τ_{22}, and τ_{33} only to avoid potential accumulation of SFS kinetic energy. The diffusion terms in Eqs. (14) and (17) are neglected because the effect of molecular diffusion is presumably much smaller than turbulence mixing. The diabatic forcing term in Eq. (14) and the microphysical forcing term in Eq. (17) are not considered in the current iGLASS to reduce its complexity. This basically means that we neglect the interaction between SFS turbulence and SFS cloud processes, which is probably not important for typical LES but may become significant in the terra incognita. How to include SFS cloud processes in iGLASS is left for future work. As mentioned earlier, the SFS covariances between θ and water variables in Eq. (15) and that between buoyancy and water variables in Eq. (17) are also neglected to maintain a manageable set of iGLASS governing equations.

With the above simplifications described, the algebraic equations of iGLASS are

$$0 = -\left(\tau_{ik}\frac{\partial\overline{u}_j}{\partial x_k} + \tau_{jk}\frac{\partial\overline{u}_i}{\partial x_k}\right) + (\delta_{i3}\tau_{Bj} + \delta_{j3}\tau_{Bi}) + \Pi_{ij} - \frac{2}{3}\delta_{ij}\epsilon, \tag{18}$$

$$0 = -\tau_{\theta j}\frac{\partial \overline{u}_i}{\partial x_j} - \tau_{ij}\frac{\partial \overline{\theta}}{\partial x_j} + 2\delta_{i3}\frac{g}{\overline{\theta}_0}e_p + \Pi_{\theta i}, \tag{19}$$

$$0 = -\tau_{qj}\frac{\partial \overline{u}_i}{\partial x_j} - \tau_{ij}\frac{\partial \overline{q}}{\partial x_j} + \Pi_{qi}, \tag{20}$$

where Π_{ij}, $\Pi_{\theta i}$, and Π_{qi} are the pressure-redistribution terms that are to be parameterized, and ϵ is the dissipation rate of SFS TKE. The model for Π_{ij} in iGLASS is based on Launder et al. (1975) and Gibson and Launder (1978), and it has four parts: slow redistribution, rapid redistribution, buoyancy effect, and wall-pressure effect, each of which is represented by a line on the right side of the expression below,

$$\begin{aligned}\Pi_{ij} = &-c_1\frac{\epsilon}{e}\left(\tau_{ij} - \frac{2}{3}\delta_{ij}e\right)\\ &- c_2\left(P_{ij} - \frac{2}{3}\delta_{ij}P\right) - c_3 S_{ij}e - c_4\left(D_{ij} - \frac{2}{3}\delta_{ij}P\right)\\ &- c_g\frac{g}{\overline{\theta}_0}\left(\delta_{j3}\tau_{\theta i} + \delta_{i3}\tau_{\theta j} - \frac{2}{3}\delta_{i3}\delta_{ij}\tau_{\theta 3}\right)\\ &+ f(z)\left[c_5\frac{\epsilon}{e}\left(\tau_{ij} - \frac{2}{3}\delta_{ij}e\right) + c_6 P_{ij} - c_7 D_{ij} + c_8 S_{ij}e\right],\end{aligned} \tag{21}$$

where

$$D_{ij} = -(\tau_{ik}\partial\overline{u}_k/\partial x_j + \tau_{jk}\partial\overline{u}_k/\partial x_i), \tag{22}$$

$$S_{ij} = \partial\overline{u}_i/\partial x_j + \partial\overline{u}_j/\partial x_i, \tag{23}$$

$$P_{ij} = -(\tau_{ik}\partial\overline{u}_j/\partial x_k + \tau_{jk}\partial\overline{u}_i/\partial x_k), \tag{24}$$

$$P = -\tau_{ij}\partial\overline{u}_j/\partial x_i, \tag{25}$$

$$f(z) = 0.27\Delta z/z. \tag{26}$$

Δz in the wall function $f(z)$ is the vertical grid spacing. The pressure redistribution terms $\Pi_{\theta i}$ and Π_{qi} are modeled similarly,

$$\Pi_{\theta i} = -c_{1s}\frac{\epsilon}{e}\tau_{\theta i} + c_{2s}\tau_{\theta k}\frac{\partial \overline{u}_i}{\partial x_k}, \tag{27}$$

$$\Pi_{qi} = -c_{1s}\frac{\epsilon}{e}\tau_{qi} + c_{2s}\tau_{qk}\frac{\partial \overline{u}_i}{\partial x_k}, \tag{28}$$

in which the first term is slow redistribution and the second term is rapid redistribution. The default model coefficients of iGLASS are shown in Table 1, which are distilled from Craft and Launder (2001), Hanjalić (2002), Launder et al. (1975), and Shabbir and Shih (1992). We tested a few alternative sets of model coefficients based on available literature but did not find significant differences for cases reported here. Therefore, iGLASS's sensitivity to model coefficients is not discussed below. However, it should be noted that the parameters chosen here may not be optimal for some other dynamic regimes.

TABLE 1. iGLASS model coefficients.

c_1	c_2	c_3	c_4	c_5	c_6	c_7	c_8	c_g	c_{1s}	c_{2s}
1.80	0.78	0.27	0.22	0.80	0.06	0.06	0.00	0.60	3.50	0.55

Two key variables in iGLASS are the SFS TKE e and TPE e_p. Though it is possible to derive diagnostic relations for them, it is better to use prognostic equations to enable SFS "memory." For example, in TI, SFS process and the resolved flow are not well separated, in which case memory terms, that is, quantities depending on the history of a flow, should arise in parameterizations (Tan et al. 2018; Ruelle 2009). The parameterized prognostic equation for SFS TKE in iGLASS is

$$\frac{De}{Dt} = \frac{1}{\hat{\rho}}\frac{\partial}{\partial x_j}\left(2\hat{\rho}K\frac{\partial e}{\partial x_j}\right) - \tau_{ij}\frac{\partial \overline{u}_i}{\partial x_j} + \tau_{B3} - \epsilon, \tag{29}$$

where an eddy diffusivity K is used to parameterize the third-order transport term. As in the conventional TKE 1.5-order closure scheme (e.g., Deardorff 1980), K is determined by

$$K = c_m l e^{1/2}, \tag{30}$$

where $c_m = 0.10$, and l is an eddy length scale,

$$l = \begin{cases} \min\left[\left(\frac{2}{3}\frac{e}{N^2}\right)^{1/2}, \Delta z\right], & N^2 > 0 \\ \Delta z, & N^2 \le 0 \end{cases}. \tag{31}$$

The squared Brunt–Väisälä frequency N^2 is determined by different expressions for saturated and subsaturated grid cells (Shi et al. 2019). Here the vertical grid spacing Δz, in lieu of the geometric-mean grid spacing $\Delta = (\Delta x\Delta y\Delta z)^{1/3}$, is used, because in TI, grid aspect ratio can become very large and using Δ would lead to significant overestimation of the eddy length scale. Ideally, this length scale should depend on horizontal grid spacing too and adapt based on the relation between grid spacing and the scales of energetic eddies (Honnert 2016; Kurowski and Teixeira 2018). Here we use Δz for simplicity in this initial implementation of iGLASS. The dissipation term ϵ is parameterized as (Moeng 1984)

$$\epsilon = c_\epsilon e^{3/2}/l, \tag{32}$$

where $c_\varepsilon = 0/2 + 0.787l/\Delta z$.

The parameterized prognostic equation for SFS TPE is

$$\frac{De_p}{Dt} = \frac{1}{\hat{\rho}}\frac{\partial}{\partial x_j}\left(2\hat{\rho}K\frac{\partial e_p}{\partial x_j}\right) - \tau_{\theta j}\frac{\partial \overline{\theta}}{\partial x_j} - \frac{e_p}{re/\epsilon}, \tag{33}$$

where the third-order transport term is again modeled with an eddy diffusivity K, which is the same as that in Eq. (29), and the last term on the right side is a simple model for the diffusion of SFS TPE following Lazeroms et al. (2016). $r = 0.55$ here and e/ϵ is the characteristic time scale of SFS velocity fluctuations.

Equations (18)–(33) represent our implementation of iGLASS, which entails integrating two prognostic equations and solving a $(9 + 3n) \times (9 + 3n)$ system of linear algebraic equations for each grid cell. The LU-decomposition algorithm (ludcmp and lubksb) provided in *Numerical Recipes in Fortran 77* by Press et al. (1992) is adopted in iGLASS for solution of the matrix.

This set of equations should result in realizable solutions, because all the simplifications make the resulting fluxes approach idealized states (e.g., quasi-equilibrium), but do not make them violate any original equations in a fundamental way. In practice, however, iGLASS solutions may cause numerical instability in simulations despite being realizable. Thus, to ensure numerical stability, it is necessary to have an additional procedure to remove physically "singular" solutions. The mathematically singular matrices corresponding to Eqs. (18)–(20) are easy to find, but such singularity rarely occurs in real atmospheric flows. The more common problem is that some of the matrices are physically "singular," meaning that the quasi-equilibrium assumption of iGLASS is locally violated and as a result, their solutions become unrealistically large in amplitude and cause numerical instability in the simulation. Therefore, for each grid cell, the absolute value of an SFS flux $|\tau|$ is compared with the median absolute values $\mathscr{M}$ of the 3×3 block of cells (at the same horizontal level) centered at that cell; if $|\tau| > 10\mathscr{M}$, we define the SFS flux at this grid cell as "singular" and replace it with the mean value of nonsingular cells in this 3×3 block. A higher threshold value, $100\mathscr{M}$ for example, can be used and would be sufficient to ensure numerical stability, but we found that a large threshold like $100\mathscr{M}$ can still allow sporadically distributed large-amplitude SFS fluxes, which do not appear to be physically reasonable. Such discontinuity in solutions might result from failures of the pressure-redistribution term in approximating the complex physics of pressure–momentum interaction, but other simplifications might also contribute to the error. This physical singularity does not occur very often in our simulations. For example, in the simulation of the stratocumulus-capped boundary layer at the standard LES resolution, only 0.6% of all grid cells are found to produce singular $\tau_{\theta 3}$ values (with $10\mathscr{M}$ as the threshold). This treatment of singularity removal can be considered a numerical regularization (cf. Gatski and Speziale 1993). Our regularization has a parallel in the clipping procedure for dynamic SGS models (Chow et al. 2005).

c. *Other closures in this study*

The other turbulence closure schemes included in this study are the Smagorinsky model (Smagorinsky 1963), the TKE 1.5-order model (Deardorff 1980), and the DRM (Chow et al. 2005). The former two models are traditional eddy diffusivity models, while the DRM employs an explicit filtering and reconstruction framework. The traditional models are entirely dissipative (diffusive), but the DRM allows backscatter of energy and scalar variance. This flexibility of DRM allows it to depict unresolved turbulence more accurately, in simulations of both dry and cloudy boundary layers (Zhou and Chow 2011, 2014; Shi et al. 2018). In the terra incognita, DRM also has other advantages compared with traditional models, such as in the representation of heterogeneity and three-dimensionality of SFS turbulence. A detailed description of these three turbulence models is provided in Shi et al. (2018). Two versions of DRM were evaluated in Shi et al. (2018). DRM-D, which uses dynamically computed eddy diffusivity for scalar transport, might be better than the DRM-Pr, which calculates eddy diffusivity by dividing the dynamically determined eddy viscosity with an empirical Prandtl number (Pr). However, to be consistent with TI results presented in (Shi et al. 2018), this study uses their DRM-Pr and employs zero-order reconstruction. For brevity, we simply refer to it as DRM in the discussion below.

3. Neutral boundary layer

We first evaluate the performance of iGLASS in the simulation of the NBL. The setup of the simulation mostly follows Chow et al. (2005) and Kirkil et al. (2012). The wind field is initialized with an analytical Ekman spiral solution and driven by a constant pressure gradient that corresponds to a geostrophic wind of $(U_g, V_g) = (10, 0)\ \mathrm{m\,s^{-1}}$. The horizontal grid spacing $\Delta x = 32$ m, and the vertical grid spacing Δz ranges between 8 and 67 m, with finer resolution near the bottom

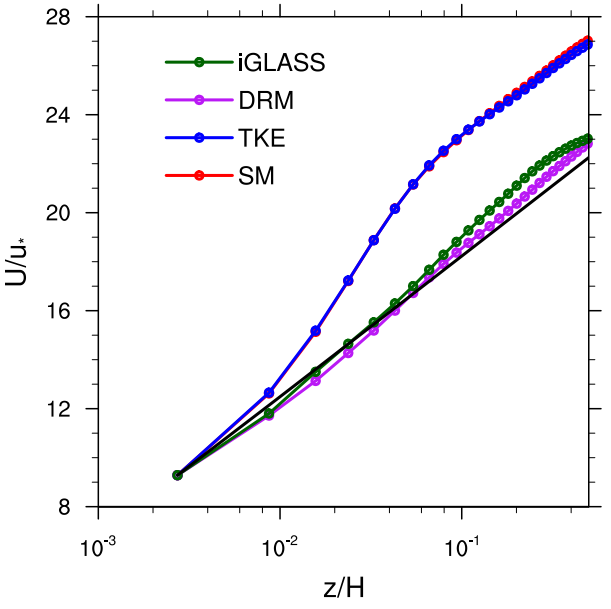

FIG. 1. Horizontal- and time-mean profiles of wind speed U in the neutral boundary layer simulations using the Smagorinsky model (SM), TKE-1.5 model, DRM, and iGLASS. The theoretical log profile is shown as the black line.

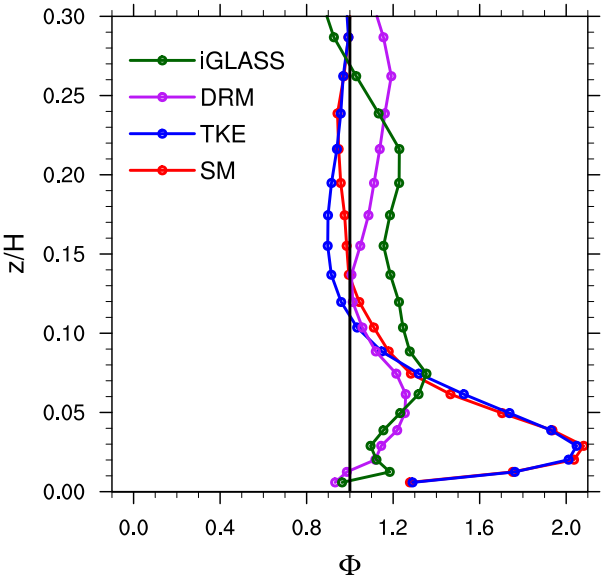

FIG. 2. Horizontal- and time-mean profiles of the nondimensional wind shear Φ in the neutral boundary layer simulations using the Smagorinsky model (SM), TKE-1.5 model, DRM, and iGLASS.

boundary. The horizontal domain size is 3456 m, and the height of the domain is 1500 m. All simulations were run for 30 physical hours, but only the data from the last 4 h were used for analysis. Because the DRM alone tends to underpredict near-surface stress due to the small sizes of near-surface eddies and the effect of numerical dissipation, the near-wall stress model of Brown et al. (2001) is used to ameliorate this problem [cf. Eq. (20) of Chow et al. (2005)]. The iGLASS also underpredicts near-surface stress because its solution is tied to resolved gradients [cf. Eqs. (18)–(20)], with errors that are too large near the surface. Thus, the same near-wall model is also applied to the iGLASS simulation. Specifically, the scaling factor C_c for the DRM and iGLASS simulations are 0.6 and 0.7, respectively, and for both of them, the near-wall model is only applied to the lowest 128 m ($4\Delta x$). This near-wall model is not used for the latter case of the stratocumulus-capped boundary layer, which is not sensitive to the details of near-surface stresses. A fifth-order weighted essentially nonoscillatory (WENO) scheme (Borges et al. 2008) is used to compute advection terms in the simulations.

Figure 1 shows the mean profiles of wind speed U, which are normalized by the mean friction velocity u_* and expected to follow the theoretical log-law profile given by Monin–Obukhov similarity theory. The height of the simulation domain is used as the boundary layer depth H. The Smagorinsky and TKE-1.5 models produce very similar results, in which the wind speed is significantly overpredicted starting from the third model level. In contrast, the DRM and iGLASS exhibit wind profiles consistent with the theoretical log-law profile. iGLASS performs slightly better than the DRM below $0.05H$, but slightly overpredicts the wind speed above compared with the DRM.

The nondimensional wind shear

$$\Phi = \frac{\kappa z}{u_*}\frac{\partial U}{\partial z}, \tag{34}$$

where $\kappa = 0.4$ is the von Kármán constant, is expected to be 1 in the logarithmic region below approximately 0.1–$0.15H$. Figure 2 shows the mean profiles of nondimensional wind shear in the simulations. Below about $0.1H$, Φ is significantly overpredicted in the Smagorinsky and TKE-1.5 models, with maximum values greater than 2, which is typical for these models (e.g., Kirkil et al. 2012). The DRM and iGLASS, in contrast, produce Φ values of about 1.2 in this region. Thus, the performance of iGLASS in the NBL simulation is much better than the traditional models and comparable to the DRM.

The difference between these turbulence models is also evident in the turbulent flow structures. Figure 3 shows instantaneous snapshots of the u component of wind at the 50-m height level. Observational results suggest that at low levels in the boundary layer, flow tends to organize as elongated streaks parallel to the

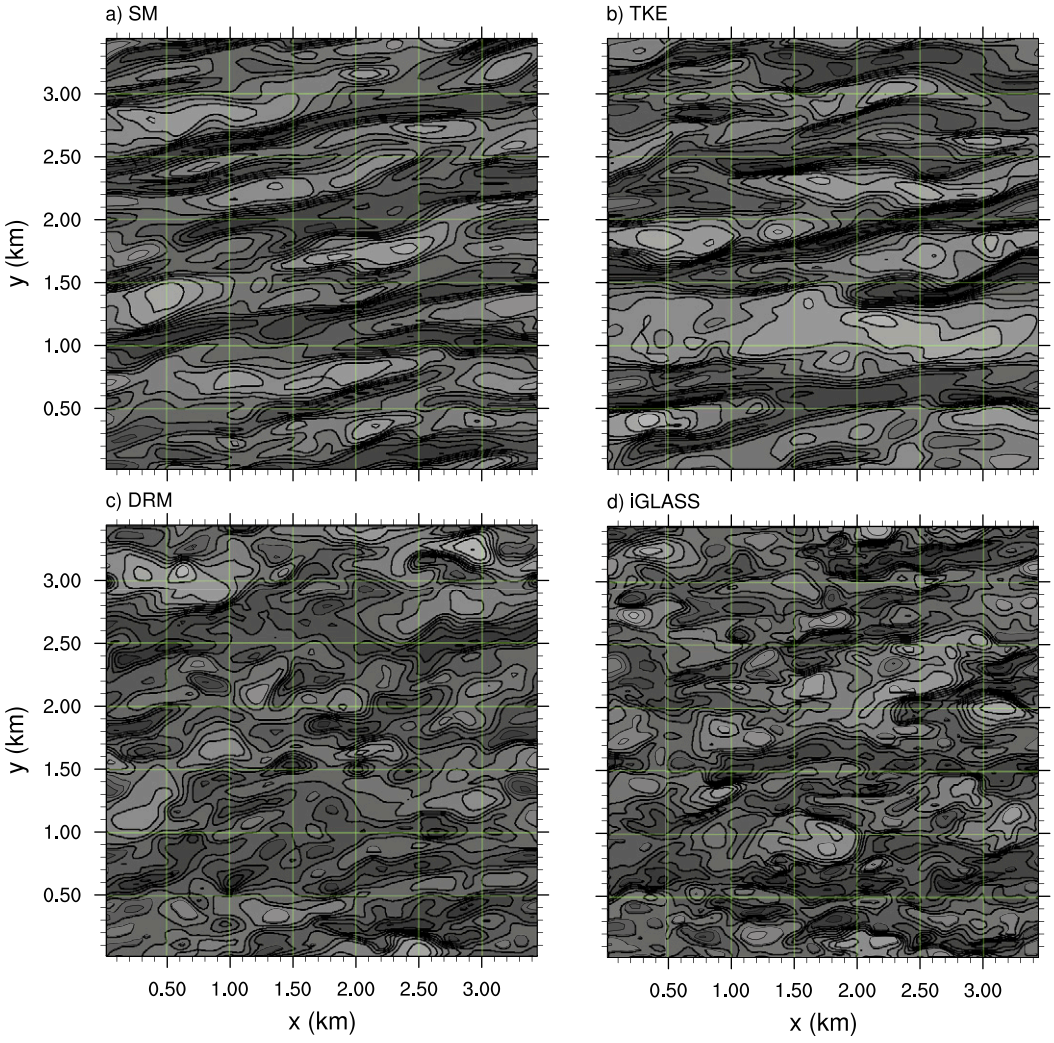

FIG. 3. Contours of instantaneous u component of wind at $z \approx 50$ m in the neutral boundary layer simulations using the (a) Smagorinsky model (SM), (b) TKE-1.5 model, (c) DRM, and (d) iGLASS.

mean wind and with a length scale of 15δ–20δ, where $\delta \approx 0.1H$ is the height of the surface layer (e.g., Hutchins and Marusic 2007). The Smagorinsky and TKE-1.5 models produce very long streaks in the simulations, while the DRM and iGLASS lead to flow fields with shorter streaks and rich in small-scale structures. The length scale of the resolved eddies in the DRM and iGLASS simulations is roughly 1000 m in Figs. 3c and 3d, consistent with previous observation and simulation results (Hutchins and Marusic 2007; Ludwig et al. 2009; Kirkil et al. 2012). Though having similar characteristic lengths, Fig. 3 suggests the iGLASS simulation has more small-scale variability in the flow than the DRM simulation.

To quantify the difference in flow structures, the energy spectra of three-dimensional wind at two different height levels are shown in Fig. 4. At both the 30- and 120-m levels, iGLASS exhibits more energy at high wavenumber modes than other turbulence models, including DRM. DRM exhibits more energy than the Smagorinsky and TKE-1.5 models at the 30-m level, but at the 120-m level, DRM exhibits slightly less energy than the traditional models at scales smaller than ~200 m. The inertial subrange, where the slope of the energy spectrum is expected to follow $k^{-5/3}$ approximately, appears at smaller scales (higher wavenumbers) in the iGLASS simulation than in others. All these interesting differences suggest that iGLASS is less dissipative than other turbulence schemes, including the DRM. Since the DRM is already a backscatter-permitting model, the energy spectra in Fig. 4 imply that iGLASS allows more backscatter than DRM, though the net effect of both models is still dissipative. As discussed in the next section, this character of

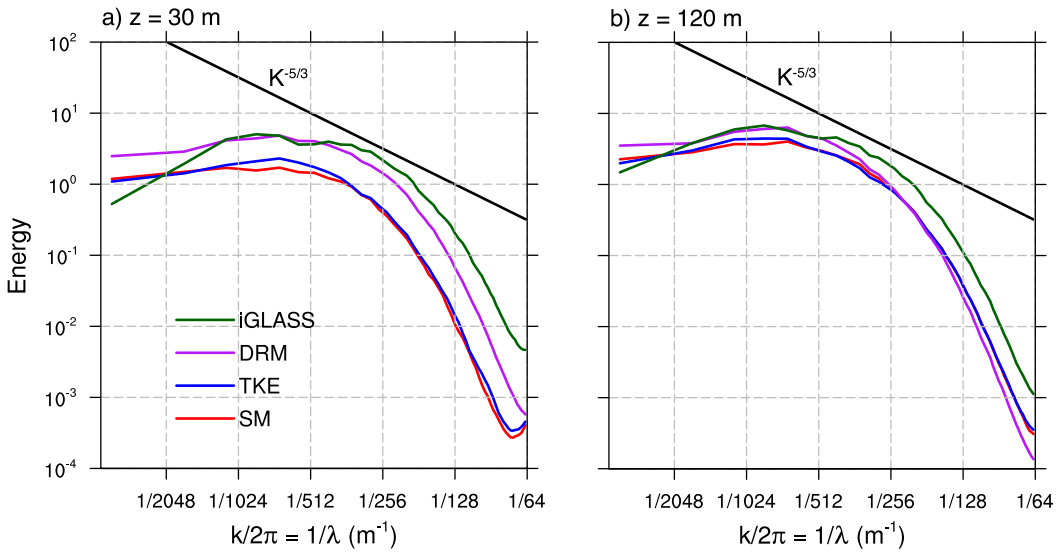

FIG. 4. Mean energy spectra of the three-dimensional wind at (a) $z = 30$ and (b) $z = 120$ m in the neutral boundary layer simulations using the Smagorinsky model (SM), TKE-1.5 model, DRM, and iGLASS. On the x axis k is the horizontal wavenumber. The energy spectrum for a given horizontal plane is computed with two-dimensional Fourier transforms of the three velocity components (u, v, w), and all spectra for the same height level are averaged in time to produce a mean spectrum of the corresponding simulation.

iGLASS is important for its superior performance in simulating the challenging case of the stratocumulus-capped boundary layer.

4. Stratocumulus-capped boundary layer

a. LES of the SCBL

Low clouds are the leading source of uncertainty in the sensitivities of global climate models (Zelinka et al. 2013; Bretherton 2015). To develop accurate parameterizations and physical understanding, LES is often employed in studies of low-cloud-capped boundary layers. In the case of stratocumulus clouds, however, LES with high resolution may still fail to reproduce observed cloud characters with sufficient fidelity because the SCBL usually involves a very sharp capping inversion and active turbulence driven by the radiative cooling at cloud top. Many LES codes may underestimate cloud fraction, turbulence strength, and boundary layer structure when simulating the SCBL (Stevens et al. 2005; Pressel et al. 2017; Shi et al. 2018).

In particular, these simulations can be very sensitive to the choice of turbulence schemes (Stevens et al. 2005). Here we evaluate iGLASS and other turbulence schemes in the LES of the challenging first research flight (RF01) case of the Second Dynamics and Chemistry of Marine Stratocumulus field study (DYCOMS II; Stevens et al. 2003). Following Stevens et al. (2005) and Shi et al. (2018), the velocity and scalar variables are initialized with semi-idealized profiles based on the observations. The horizontal grid spacing is 35 m, and the vertical grid spacing is 5 m. The horizontal domain size is 3360 m in both the x and y directions and the domain height is 1500 m. We ran CM1 with different turbulence schemes for 4 h, but only the data from the last hour were used for analysis. Again, the fifth-order WENO scheme is used to compute the advection of velocity and scalars. The microphysical processes are represented with the Morrison double-moment scheme (Morrison et al. 2005). More details about the setup of this case are provided in Shi et al. (2018). The boundary layer height in this case is approximately 840 m, and cloud exists between 600 m and the top of the boundary layer. Cloud cover in this case is nearly 100% during the observation period.

Figure 5 shows the mean profiles of cloud water mixing ratio q_c and liquid water potential temperature θ_l. The initial conditions and observed values are also shown in the figure. Compared with the Smagorinsky and TKE-1.5 models, DRM and iGLASS predict significantly more cloud water and match observations better. The SCBL is usually well mixed, thus θ_l is expected to be uniform below the cloud top. However, the Smagorinsky model produces a weak gradient in θ_l in the cloud layer. The TKE-1.5 model also exhibits a noticeable, though very weak, gradient. In contrast, the DRM and iGLASS simulations exhibit uniform profiles of θ_l below the cloud top.

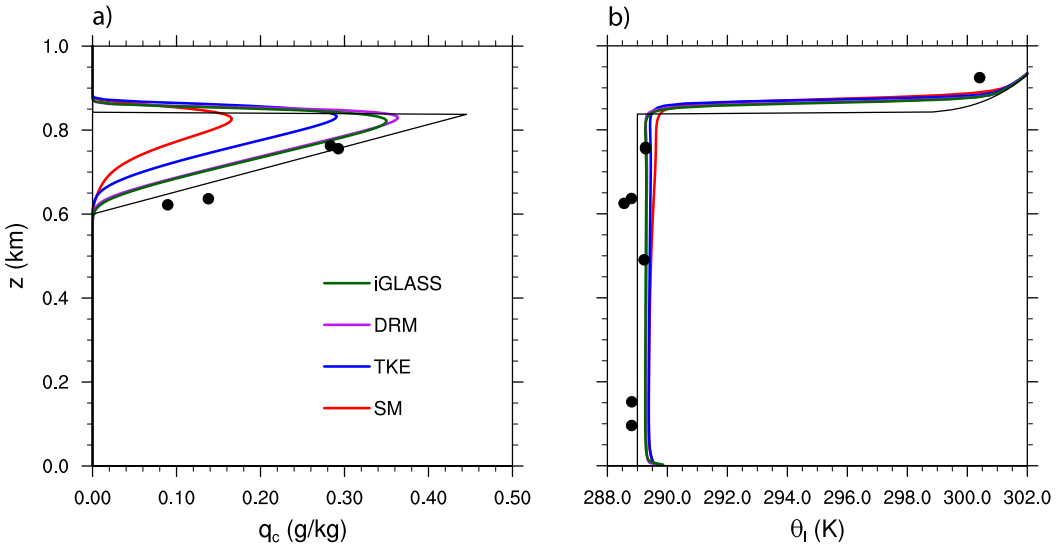

FIG. 5. Horizontal- and time-mean profiles of (a) cloud water mixing ratio q_c and (b) liquid water potential temperature θ_l in the SCBL simulations with 35-m horizontal and 5-m vertical grid spacings. The black lines indicate the initial conditions of q_c and θ_l. The black dots indicate observed values during DYCOMS II RF01 (Stevens et al. 2005).

The variance and third moment of the resolved vertical velocity are shown in Fig. 6. The observation indicates the variance profile should have one single peak around the cloud base ($z \sim 600$ m), which suggests the SCBL is vertically coupled. The Smagorinsky model produces a decoupled boundary layer with double peaks and reduced strength of vertical motions. The TKE-1.5 model appears to exhibit a single-peak structure, but the intensity of vertical motions is relatively weak. The DRM and iGLASS exhibit well-defined single-peak structure in the variance profile and strong vertical motions, matching observation data significantly better. iGLASS appears to perform slightly better than the DRM in that its vertical motions are stronger than those in the DRM simulation.

The third moment of the vertical velocity is also helpful in describing the characteristics of the turbulent motions in the boundary layer. As shown in Fig. 6b,

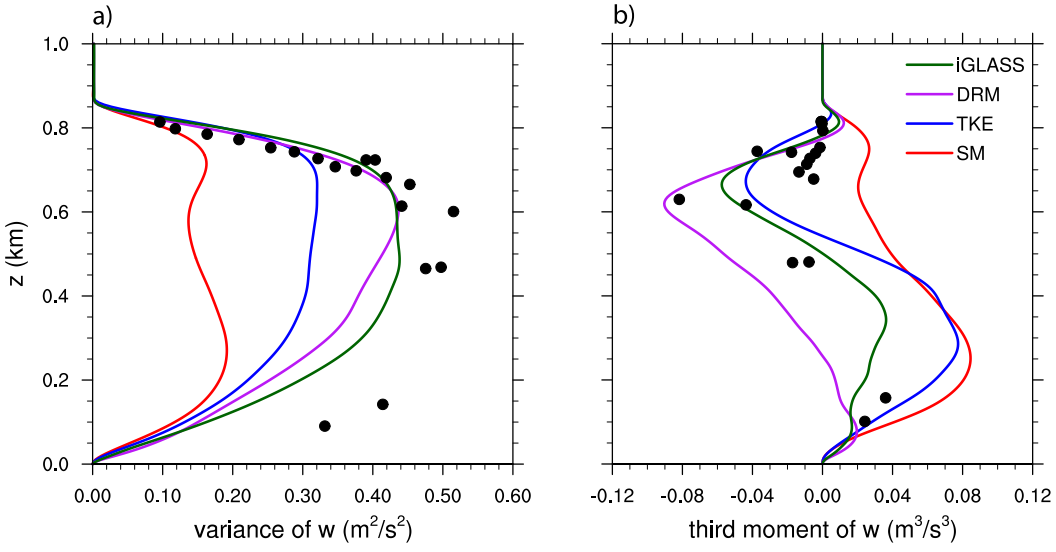

FIG. 6. Horizontal- and time-mean profiles of (a) the variance and (b) the third moment of the resolved vertical velocity $\overline{w}$ in the SCBL simulations with 35-m horizontal and 5-m vertical grid spacings. The black dots indicate observed values during DYCOMS II RF01 (Stevens et al. 2005).

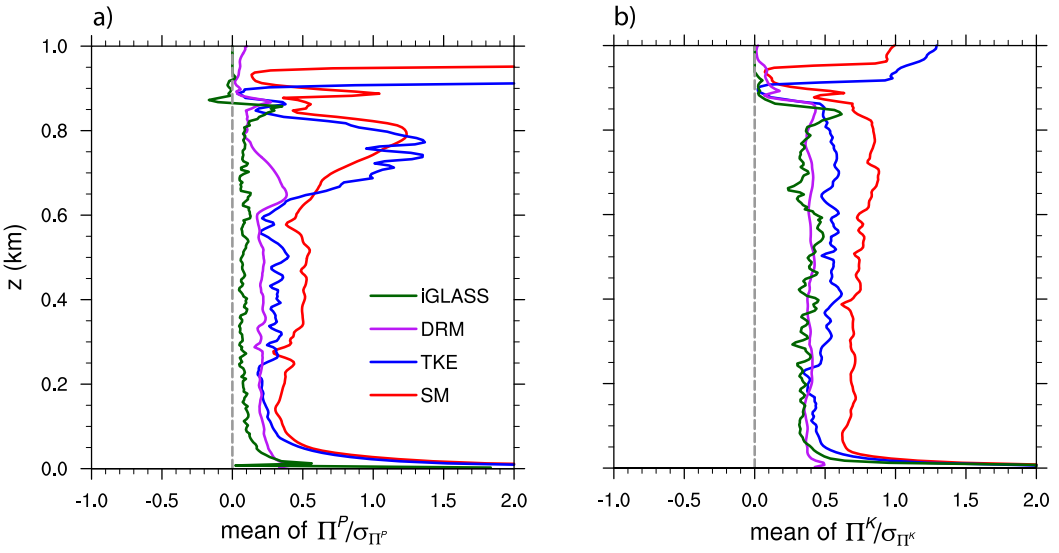

FIG. 7. Horizontal- and time-mean profiles of normalized scale-transfer rate of (a) turbulence potential energy Π^P and (b) turbulence kinetic energy Π^K. They represent the transfer rate of energy from resolved scales to subfilter scales and are normalized by the standard deviation of the transfer rates σ_{Π^P} and σ_{Π^K}, respectively.

the observation data indicate the presence of a negative peak around the cloud base, which suggests the flow is dominated by narrow, strong downdraft plumes driven by radiative cooling at the cloud top and accompanied by wide, gentle upward motions. The DRM, iGLASS, and TKE-1.5 capture this negative-peak structure in their simulations, but the profiles of the Smagorinsky model is dominated by a positive peak at lower levels, which suggests turbulent motions are driven primarily by surface heating. Again, iGLASS appears to perform slightly better than the DRM in that the DRM overpredicts the negative third-moment values moderately.

Shi et al. (2018) suggested that the key to producing satisfying performance in the simulation of the SCBL is a turbulence scheme's capability to represent backscatter, that is, countergradient fluxes of momentum and scalars, appropriately. This occurs because modeled backscatter reduces the entrainment of warm, dry air at

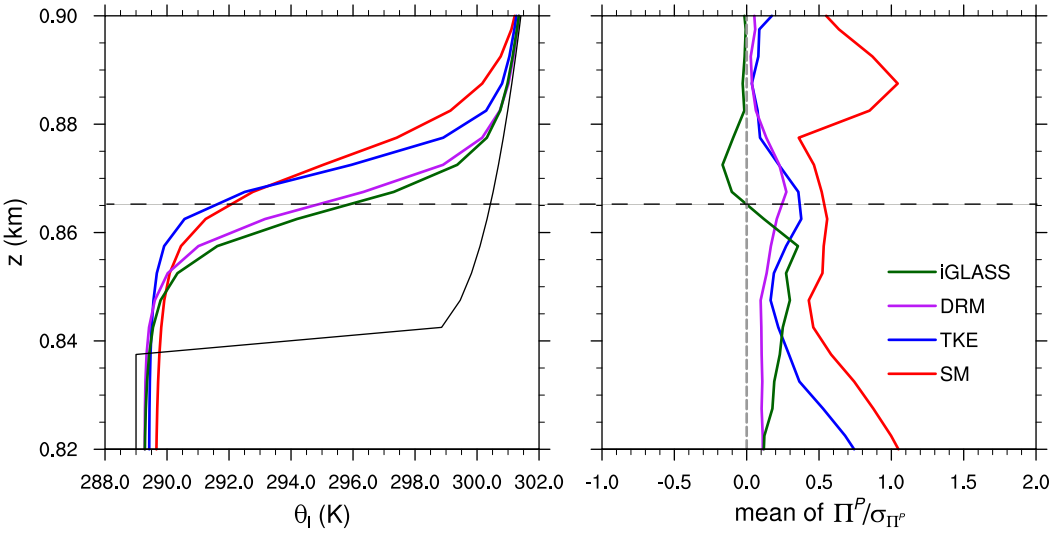

FIG. 8. Horizontal- and time-mean profiles of (left) liquid water potential temperature θ_l and (right) normalized scale-transfer rate of turbulence potential energy Π^P around the inversion layer. The solid black curve in the left panel is the θ_l profile in the initial condition. The dashed horizontal lines in both panels indicate the height at which the planar-averaged Π^P is zero in the iGLASS simulation.

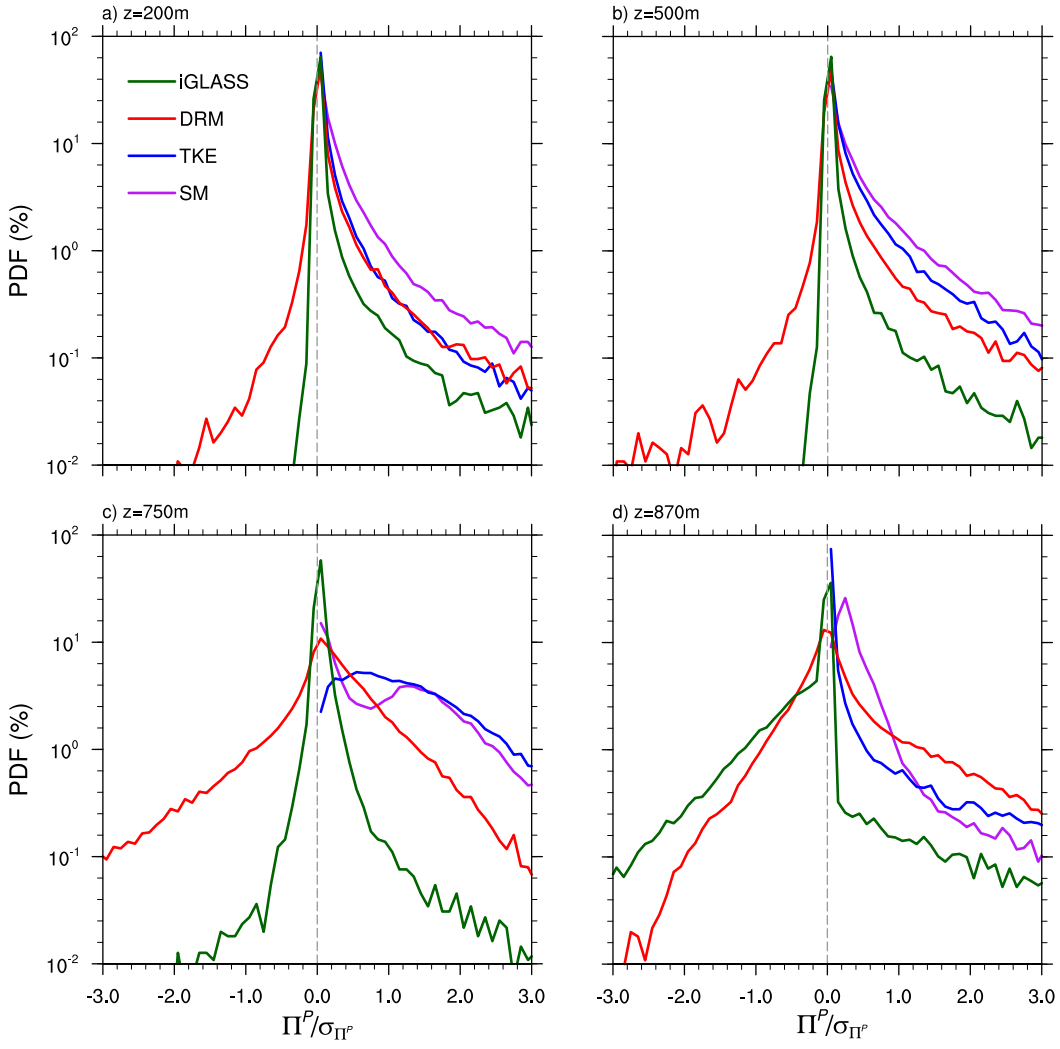

FIG. 9. Probability distribution function (PDF) of the scaled transfer rate Π^P at different levels. On the x axis σ_{Π^P} is the standard deviation of the transfer rates. Data from hour 4 of the simulations are used to compute Π^P.

the cloud top and preserves turbulence potential and kinetic energy in the boundary layer driven by radiative cooling. Traditional turbulence closure schemes, such as the Smagorinsky and TKE-1.5 models, are entirely dissipative/diffusive so that dry, warm air from the free troposphere can intrude into the cloud layer easily and turbulence energy at the resolved scales is dissipated before actually mixing the boundary layer.

The transfer rate of turbulence potential energy and kinetic energy from the resolved scales to subfilter scales can be measured by $\Pi^P = -\tau_{\theta j}\partial\overline{\theta}/\partial x_j$ and $\Pi^K = -\tau_{ij}\overline{S}_{ij}$, respectively [cf. Eq. (18) of Shi et al. (2018)]. Figure 7 shows the mean profiles of normalized Π^P and Π^K, for which larger, positive values indicate stronger dissipation. In general, the Smagorinsky and TKE-1.5 models are more dissipative than the DRM and iGLASS. The difference is most dramatic in the cloud layer for Π^P, which exhibits relatively large, positive values for the traditional schemes but is close to zero in the DRM and iGLASS simulations. iGLASS appears to be slightly less dissipative than the DRM. This probably is the reason that iGLASS performs better than the DRM in terms of vertical velocity statistics. Intriguingly, Π^P for iGLASS is negative at the cloud top ($z = 875$ m). This height is within the narrow capping inversion, which strongly suppresses the occurrence of turbulent mixing. To examine this iGLASS behavior, Fig. 8 shows an expanded view of θ_l and normalized Π^P around the inversion. Close examination of $\tau_{\theta j}$ (not shown) reveals that in the iGLASS simulation, $\tau_{\theta 3}$ dominates and smoothly approaches zero with increasing height going through the inversion. In the DRM simulation, $\tau_{\theta 3}$ also dominates and weakens with height near the inversion, though it is significantly

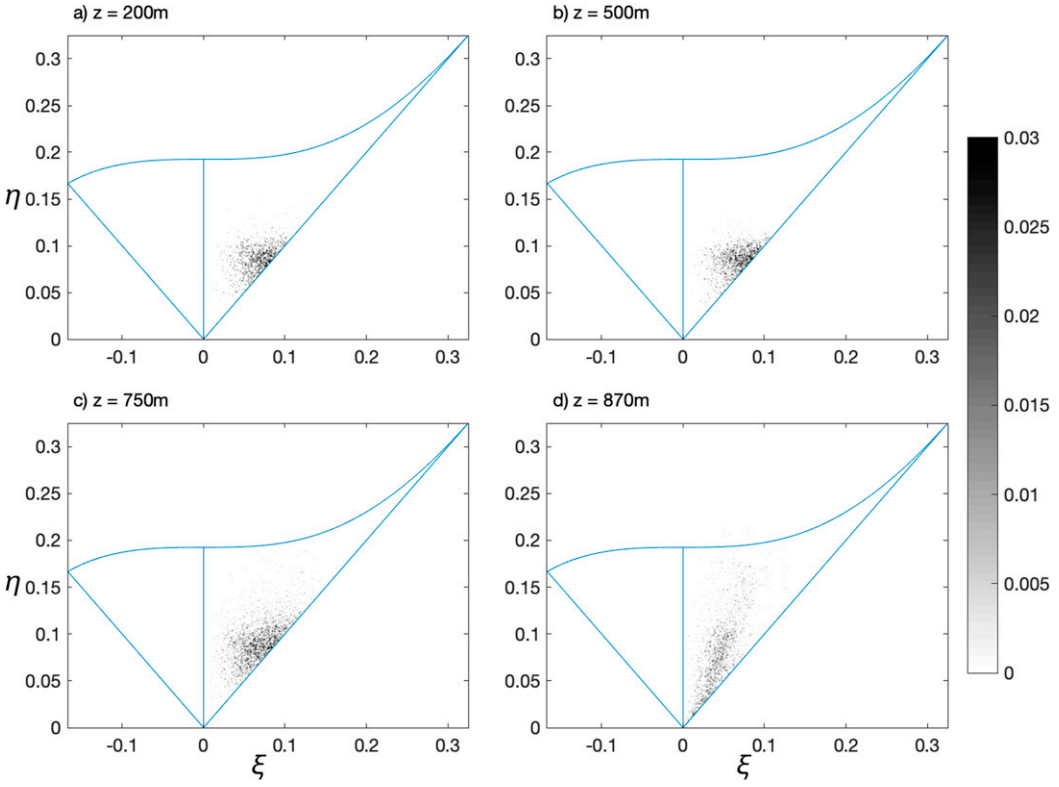

FIG. 10. Lumley triangle (blue curves) and the frequency distribution (%; indicated by the gray scale) of the invariants η and ξ in iGLASS simulation of the SCBL. Four different height levels are shown here as indicated by panel labels. Data from the last time slice are used for the analysis. Bin widths of η and ξ used in the analysis are 0.001.

stronger than the values in iGLASS. Instantaneous snapshots of $\tau_{\theta 3}$ (not shown) show that in the middle of the inversion (~870 m), $\tau_{\theta 3}$ of iGLASS is close to zero over almost all of the horizontal extent of the domain, except for in a few areas where iGLASS produces noticeable upward heat fluxes. In contrast, DRM exhibits significantly stronger upward and downward θ flux at the same height level with the horizontally averaged flux being downward.

The probability distribution functions (PDFs) of these terms elucidate the primary reason for these differences. Figure 9 shows the PDFs of Π^P at different height levels. As expected, the Smagorinsky and TKE-1.5 models can only produce forward scatter (positive values). In the subcloud layer (Figs. 9a,b), iGLASS mainly produces forward scatter, though with strength weaker than other models. Its backscatter is almost negligible compared with the backscatter of DRM. Within the cloud layer (Fig. 9c), iGLASS exhibits a more symmetric distribution compared with its PDFs at the subcloud levels. However, at the cloud top within the inversion layer (Fig. 9d), iGLASS exhibits stronger backscatter than forward scatter, resulting in countergradient mixing overall. Therefore, iGLASS appears to be a model with more flexibility in adapting SFS stress and fluxes to different flow regimes than other schemes including DRM. iGLASS can behave like a weakly dissipative/diffusive model in some regions of the flow, while also being able to produce backscatter mainly in other regions. Whether iGLASS is actually representing the detailed SFS mixing more accurately than DRM will require further field observation of microscale flows.

Another issue to consider is the realizability of iGLASS. This can be done by investigating the invariants of the SFS anisotropy tensor and comparing them against the Lumley triangle (Lumley 1979; Pope 2000). The anisotropy tensor is defined as

$$b_{ij} = \frac{\tau_{ij}}{\tau_{kk}} - \frac{1}{3}\delta_{ij}. \tag{35}$$

Because b_{ij} is traceless, the three eigenvalues of it, λ_1, λ_2, and λ_3 satisfy $\lambda_1 + \lambda_2 + \lambda_3 = 0$. Thus, only two invariants are needed to sufficiently describe b_{ij}. Following Pope (2000), these two invariants (ξ, η) are defined as

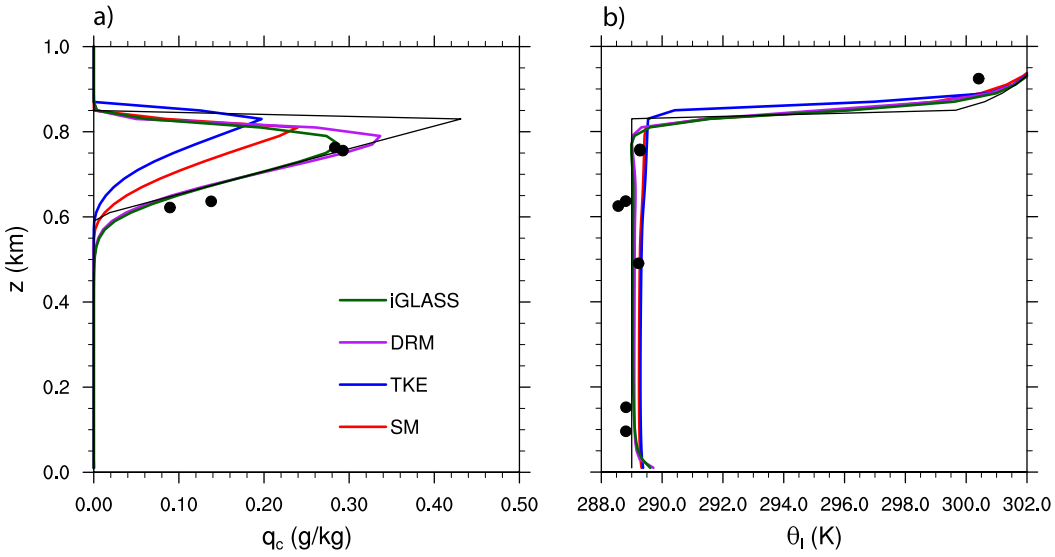

FIG. 11. Horizontal- and time-mean profiles of (a) cloud water mixing ratio q_c and (b) liquid water potential temperature θ_l in the SCBL simulations with 1-km horizontal and 20-m vertical grid spacing. The black lines indicate the initial conditions of q_c and θ_l. The black dots indicate observed values during DYCOMS II RF01 (Stevens et al. 2005).

$$\eta^2 = \frac{1}{3}(\lambda_1^2 + \lambda_1\lambda_2 + \lambda_2^2) \tag{36}$$

and

$$\xi^3 = -\frac{1}{2}\lambda_1\lambda_2(\lambda_1 + \lambda_2). \tag{37}$$

Special states of turbulence flux form the so-called Lumley triangle, which is indicated by blue curves in Fig. 10. All realizable sets of η and ξ should fall within the triangle. The pairs that fall within the left half of the triangle indicate SFS tensors dominated by two dimensions (pancake like), and the pairs that fall within the right half indicate tensors stretched in one direction (cigar like). Statistics of the iGLASS anisotropy tensor (gray shaded area in Fig. 10) suggest the SFS flux from iGLASS is always dominated by one dimension. All pairs of (ξ, η) fall on the right half of the Lumley triangle, close to the leg of $\xi = \eta$ but within the triangle. For most levels, the invariants appear in a semicircular region around $\xi = \eta \approx 0.85$. However, for the level in the inversion layer ($z = 870$ m), ξ and η exhibit much larger variability. This is probably related to strong gradients in the inversion layer and formation of new eddies due to cloud-top cooling.

Therefore, solutions of the iGLASS model represent realizable turbulence fluxes. Analysis of Horizontal Array Turbulence Study (HATS) data by Sullivan et al. (2003) showed that in most cases the invariant pair falls close to (but not exactly on) the right edge ($\xi = \eta$) of the Lumley triangle, except in the situation where the flow is strongly stable. Thus, the result of the iGLASS model are consistent with HATS observation data. It is not surprising that iGLASS fluxes satisfy the realizability condition because, though simplifications were applied, iGLASS is still based on the governing equations of SFS fluxes. Excluding the "singularity removal" procedure described in section 2b does not change Fig. 10 in a noticeable way.

b. *TI of the SCBL*

Simulating the SCBL in TI is of practical importance because of the critical role played by stratocumulus clouds in the climate system (Bretherton 2015). In this section, we simulate the SCBL at much coarser resolution than in the previous section. The horizontal grid spacing used here is 1 km, and the vertical grid spacing is 20 m. The height of the domain is still 1.5 km, but the horizontal domain size is enlarged to 96 km × 96 km, using the same number of grid cells (96 × 96) in the horizontal. Other aspects of the simulation setup are the same as in the previous section.

Figure 11 compares the distribution of cloud water and liquid water potential temperature in TI-resolution simulations. The Smagorinsky and TKE-1.5 models again significantly underpredict cloud water compared with the DRM and iGLASS. Interestingly, the TKE-1.5 model, which performs better than the Smagorinsky model at the LES resolution, now appears to be slightly inferior than the Smagorinsky model (Fig. 11a).

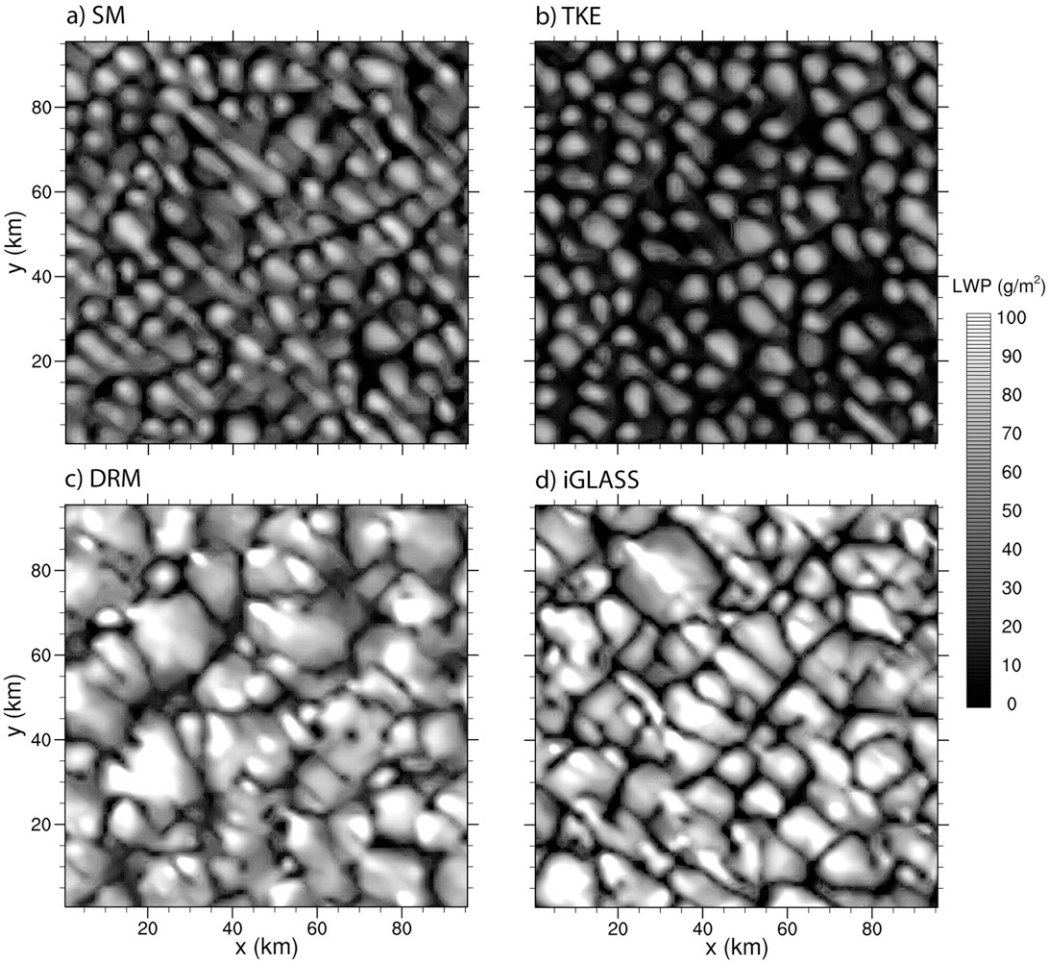

FIG. 12. Instantaneous distribution of liquid water path (LWP) at the end of TI-resolution simulations, which use different turbulence closure schemes.

The distribution of liquid water potential temperature also suggests that the DRM and iGLASS are significantly better than the traditional models, which exhibit notable θ_l gradients in the cloud layer and a weak warm bias throughout the boundary layer (Fig. 11b).

Although the maximum values of cloud water mixing ratio in Fig. 11a are not dramatically different among the different simulations, those profiles actually correspond to very different cloud types. The instantaneous distributions of liquid water path at the end of the simulations are shown in Fig. 12. The clouds in the Smagorinsky and TKE-1.5 simulations exhibit characteristics of shallow cumulus convection, in which the cloud fraction is relatively low and cloud cells are small and sporadically distributed, whereas the DRM and iGLASS simulations exhibit high cloud fractions and larger, compactly distributed cloud cells, which are more like the real-world stratocumulus. Since low cloud–radiation feedback can affect the organization of deep convection (Muller and Held 2012), the different cloud patterns seen in Fig. 12 can potentially alter the properties of other cloud and weather systems in simulations that cover much larger domains.

As mentioned in the previous section, the capability of iGLASS and DRM to produce backscatter likely plays a key role in improving the simulation of the SCBL. However, a parameterization scheme sometimes represents SFS processes at a pragmatic level but not at a precise level. Figure 13 shows scaled TPE transfer rate from resolved to unresolved scales. For Fig. 13b, the computation is the same as that for Fig. 9, in which SFS fluxes from turbulence models are used. Figure 13a shows the distribution "expected" according to LES runs discussed in the previous section. The LES data are first filtered with a moving-average filter that has a width of 1 km in the horizontal and 20 m in the vertical, that is, the sizes of TI simulation grid. Then the *expectation* of SFS θ flux in TI runs can be estimated as

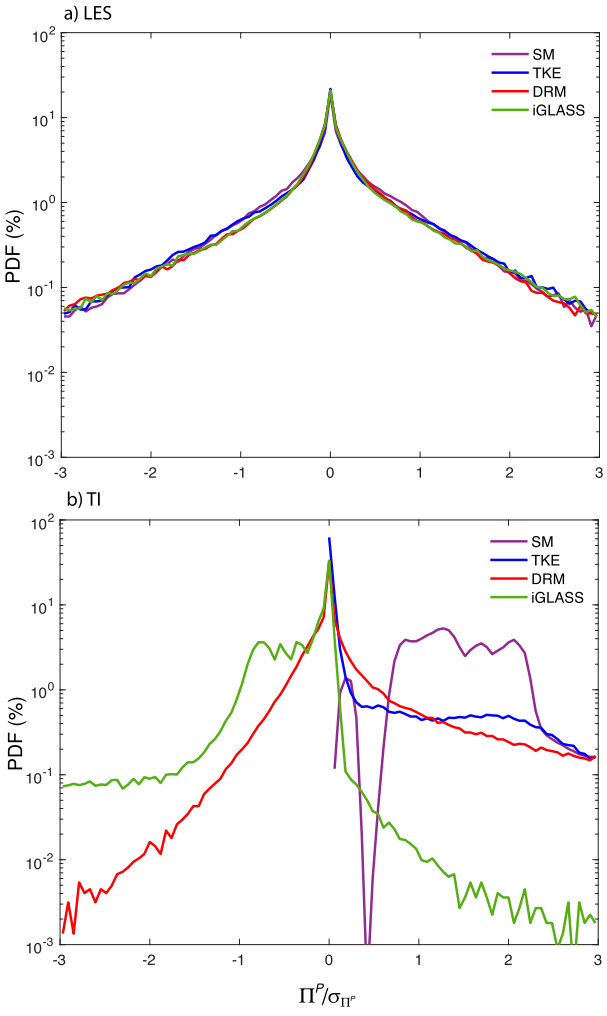

FIG. 13. Probability distribution function (PDF) of (a) the "expected" dissipation rate Π^P/σ_{Π^P} based on LESs and (b) true dissipation rate by SFS fluxes in TI simulations. Here $\Pi^P = -\tau_{\theta 3}\partial\overline{\theta}/\partial z$; i.e., only the vertical component is considered; σ_{Π^P} is the standard deviation of the transfer rates. In (a) Π^P is obtained by filtering LES data (section 2b) with a moving-average filter whose width is the same as TI grid, e.g., $\tau_{\theta 3} = \widetilde{w\theta} - \tilde{w}\tilde{\theta}$, where the tilde is the moving-average filter. Data at the z = 870-m level from hour 4 of the simulations are used.

$\tau_{\theta j} = \widetilde{\theta u_j} - \tilde{\theta}\tilde{u}_j$, where the tilde denotes the moving average filter. Corresponding gradients are also calculated using the filtered LES data. We found that the LES data suggest that the SFS component should produce backscatter at a significant fraction of grid points when coarsened to TI resolution (Fig. 13a). Figure 13b shows that traditional turbulence models cannot produce backscatter and erroneously show a plateau at positive dissipation rates (on the right half of the figure), whereas DRM and iGLASS produce backscatter as well as forward scatter, although, iGLASS seems to overproduce countergradient flux. Thus, in a qualitative sense, iGLASS and DRM are able to produce more realistic SFS flux distributions, which likely plays a key role in their superior performance.

5. Summary and discussion

The resolution of operational numerical weather forecast and regional climate simulation is moving into the terra incognita, where subfilter-scale turbulence plays active roles in the development of cloud and weather systems in simulations. Challenges in turbulence parameterization arise in this regime because many traditional assumptions about turbulence in atmospheric modeling, such as quasi-equilibrium state, horizontal homogeneity, and forward scattering, are not valid in terra incognita.

In this study, we advanced the idea of using algebraic turbulence closures and presented an improved version of iGLASS. It includes the time tendency of SFS turbulence kinetic and potential energy so as to retain "memory" of the SFS turbulence properties. Yet it does not adopt the assumption of horizontal homogeneity, thus differing from the Mellor–Yamada-type PBL schemes. iGLASS computes three-dimensional SFS mixing and does not produce explicit expressions that are equivalent to eddy-diffusivity models. Since the quasi-equilibrium assumption and other simplifications are applied to the equations of individual SFS stress/flux components and could be violated in some special situations, iGLASS may occasionally give physically singular solutions that cause numerical instability. A simple singularity detection and removal procedure is included in the new iGLASS to ensure the stability of model integration in all dynamic regimes.

Our evaluations in this study suggest that iGLASS is significantly better than the traditional models at both standard LES resolutions and at TI resolutions. iGLASS can produce a near-surface wind profile that matches the theoretical log-law profile well in the simulation of the neutral boundary layer and maintain realistic cloud distribution and active turbulence in the case of the stratocumulus-capped boundary layer. Its performance is comparable to the DRM in general and may even be slightly better than the DRM by some specific measures. Most notably, we found that iGLASS permits more net backscatter than the DRM in some regions of the flow. This is important for the simulations in the terra incognita, because modeling backscatter, in addition to modeling the usual forward scatter, is essential when turbulent eddies are partially resolved (Verrelle et al. 2017; Shi et al. 2018, 2019). As indicated by its governing equations [Eqs. (18)–(33)], iGLASS fluxes are coupled to gradients of momentum and scalars

at the resolved scales, and physically, backscatter means inverse cascade of kinetic and potential energy. Thus, in the SCBL case, backscatter is stronger near the cloud top probably because that is the region where small-scale eddies are active and energy is generated (by cloud-top cooling). Whether or not the advantages of iGLASS shown in this study can be leveraged in the simulation of other weather regimes, for example for shallow cumulus convection, needs further investigation.

Implicit algebraic turbulence closure, as represented by iGLASS here, is an attractive approach to represent SFS turbulence in the terra incognita. Key characteristics of turbulence, such as anisotropy and backscatter, are included naturally based on the governing equations of the underlying physics. The DRM, though relying on the Navier–Stokes equations ultimately, is based on the framework of explicit filtering and reconstruction, and therefore relies mainly on mathematical techniques. iGLASS can potentially connect turbulence and microphysics schemes, if SFS variability of microphysical processes need to be considered. However, the computational cost of the current version of iGLASS can increase substantially as the number of water and other chemical variables increases. For example, in the SCBL case in this study, which includes liquid cloud water and water vapor only in the microphysics module, iGLASS increases the computational cost of the simulation by about 20% compared with the traditional models, and the DRM causes a similar increase. However, if all of the 10 cloud species in the Morrison double-moment scheme are active, iGLASS can increase the computational cost of a simulation by about 150%. In contrast, the version of DRM used in this study would not have a different computational cost because it uses a Prandtl number to determine scalar eddy diffusivities. If separate dynamic procedures are applied to scalars independently with DRM, the resulting increase would be just 50%, which is significantly less than the iGLASS increase. This undesirable increase in the computational cost of iGLASS may be reduced by computing the SFS flux of total water only in iGLASS and partitioning it into the flux for individual cloud species afterward. The effects of the neglected high-order closure terms on iGLASS may also need to be discussed in future studies. Nonetheless, these initial results demonstrate iGLASS can provide a useful physics-based framework for developing appropriate turbulence closure schemes for the terra incognita.

Acknowledgments. This research was supported by National Science Foundation (NSF) Grants AGS-1503860 and AGS-1503885, and Cooperative Agreement 1852977. XS also thanks the support of HKUST startup funds. We would like to acknowledge high-performance computing support from Cheyenne (doi:10.5065/D6RX99HX) provided by NCAR's Computational and Information Systems Laboratory, sponsored by the NSF.

REFERENCES

Borges, R., M. Carmona, B. Costa, and W. S. Don, 2008: An improved weighted essentially non-oscillatory scheme for hyperbolic conservation laws. *J. Comput. Phys.*, **227**, 3191–3211, https://doi.org/10.1016/j.jcp.2007.11.038.

Bretherton, C. S., 2015: Insights into low-latitude cloud feedbacks from high-resolution models. *Philos. Trans. Roy. Soc.*, **373A**, 20140415, https://doi.org/10.1098/RSTA.2014.0415.

Brown, A. R., J. Hobson, and N. Wood, 2001: Large-eddy simulation of neutral turbulent flow over rough sinusoidal ridges. *Bound.-Layer Meteor.*, **98**, 411–441, https://doi.org/10.1023/A:1018703209408.

Bryan, G. H., and J. M. Fritsch, 2002: A benchmark simulation for moist nonhydrostatic numerical models. *Mon. Wea. Rev.*, **130**, 2917–2928, https://doi.org/10.1175/1520-0493(2002)130<2917:ABSFMN>2.0.CO;2.

——, and R. Rotunno, 2009: The maximum intensity of tropical cyclones in axisymmetric numerical model simulations. *Mon. Wea. Rev.*, **137**, 1770–1789, https://doi.org/10.1175/2008MWR2709.1.

Ching, J., R. Rotunno, M. LeMone, A. Martilli, B. Kosovic, P. Jimenez, and J. Dudhia, 2014: Convectively induced secondary circulations in fine-grid mesoscale numerical weather prediction models. *Mon. Wea. Rev.*, **142**, 3284–3302, https://doi.org/10.1175/MWR-D-13-00318.1.

Chow, F. K., R. L. Street, M. Xue, and J. H. Ferziger, 2005: Explicit filtering and reconstruction turbulence modeling for large-eddy simulation of neutral boundary layer flow. *J. Atmos. Sci.*, **62**, 2058–2077, https://doi.org/10.1175/JAS3456.1.

Craft, T., and B. Launder, 2001: Principles and performance of TCL-based second-moment closures. *Flow Turbul. Combust.*, **66**, 355–372, https://doi.org/10.1023/A:1013514632684.

Deardorff, J. W., 1974: Three-dimensional numerical study of the height and mean structure of a heated planetary boundary layer. *Bound.-Layer Meteor.*, **7**, 81–106, https://doi.org/10.1007/BF00224974.

——, 1980: Stratocumulus-capped mixed layers derived from a three-dimensional model. *Bound.-Layer Meteor.*, **18**, 495–527, https://doi.org/10.1007/BF00119502.

Ďurán, I. B., J.-F. Geleyn, F. Váňa, J. Schmidli, and R. Brožková, 2018: A turbulence scheme with two prognostic turbulence energies. *J. Atmos. Sci.*, **75**, 3381–3402, https://doi.org/10.1175/JAS-D-18-0026.1.

Enriquez, R. M., 2013: Subgrid-scale turbulence modeling for improved large-eddy simulation of the atmospheric boundary layer. Ph.D. thesis, Stanford University, 207 pp.

——, and R. L. Street, 2014: Large-eddy simulation of the stable boundary layer: Revisiting GABLS with a linear algebraic subgrid-scale turbulence model. *21st Symp. on Boundary Layers and Turbulence*, Leeds, UK, Amer. Meteor. Soc., 14.B3, https://ams.confex.com/ams/21BLT/webprogram/Manuscript/Paper247488/EnriquezStreet2014BLT.pdf.

——, F. Chow, R. Street, and F. Ludwig, 2010: Examination of the linear algebraic subgrid-scale stress [LASS] model, combined with reconstruction of the subfilter-scale stress, for large eddy

simulation of the neutral atmospheric boundary layer. *19th Symp. on Boundary Layers and Turbulence*, Keystone, CO, Amer. Meteor. Soc., 3A.3, https://ams.confex.com/ams/pdfpapers/172319.pdf.

——, ——, ——, and ——, 2012: Assessment of a coupled momentum and passive scalar flux subgrid-scale turbulence model for large-eddy simulation of the flow in the planetary boundary layer. *20th Symp. on Boundary Layers and Turbulence*, Boston, MA, Amer. Meteor. Soc., P1.45, https://ams.confex.com/ams/20BLT18AirSea/webprogram/Manuscript/Paper209117/Enriquez2012BLT.pdf.

Favre, A., 1983: Turbulence: Space-time statistical properties and behavior in supersonic flows. *Phys. Fluids*, **26**, 2851–2863, https://doi.org/10.1063/1.864049.

Findikakis, A. N., and R. L. Street, 1979: An algebraic model for subgrid-scale turbulence in stratified flows. *J. Atmos. Sci.*, **36**, 1934–1949, https://doi.org/10.1175/1520-0469(1979)036<1934:AAMFSS>2.0.CO;2.

Gatski, T. B., and C. G. Speziale, 1993: On explicit algebraic stress models for complex turbulent flows. *J. Fluid Mech.*, **254**, 59–78, https://doi.org/10.1017/S0022112093002034.

Gibson, M. M., and B. E. Launder, 1978: Ground effects on pressure fluctuations in the atmospheric boundary layer. *J. Fluid Mech.*, **86**, 491–511, https://doi.org/10.1017/S0022112078001251.

Hagelin, S., J. Son, R. Swinbank, A. McCabe, N. Roberts, and W. Tennant, 2017: The Met Office convective-scale ensemble, MOGREPS-UK. *Quart. J. Roy. Meteor. Soc.*, **143**, 2846–2861, https://doi.org/10.1002/qj.3135.

Hanjalić, K., 2002: One-point closure models for buoyancy-driven turbulent flows. *Annu. Rev. Fluid Mech.*, **34**, 321–347, https://doi.org/10.1146/annurev.fluid.34.082801.161035.

Hatlee, S. C., and J. C. Wyngaard, 2007: Improved subfilter-scale models from the HATS field data. *J. Atmos. Sci.*, **64**, 1694–1705, https://doi.org/10.1175/JAS3909.1.

Honnert, R., 2016: Representation of the grey zone of turbulence in the atmospheric boundary layer. *Adv. Sci. Res*, **13**, 63–67, https://doi.org/10.5194/ASR-13-63-2016.

Hutchins, N., and I. Marusic, 2007: Evidence of very long meandering features in the logarithmic region of turbulent boundary layers. *J. Fluid Mech.*, **579**, 1–28, https://doi.org/10.1017/S0022112006003946.

Kirkil, G., J. Mirocha, E. Bou-Zeid, F. K. Chow, and B. Kosović, 2012: Implementation and evaluation of dynamic subfilter-scale stress models for large-eddy simulation using WRF. *Mon. Wea. Rev.*, **140**, 266–284, https://doi.org/10.1175/MWR-D-11-00037.1.

Kurowski, M. J., and J. Teixeira, 2018: A scale-adaptive turbulent kinetic energy closure for the dry convective boundary layer. *J. Atmos. Sci.*, **75**, 675–690, https://doi.org/10.1175/JAS-D-16-0296.1.

Launder, B. E., G. J. Reece, and W. Rodi, 1975: Progress in the development of a Reynolds-stress turbulence closure. *J. Fluid Mech.*, **68**, 537–566, https://doi.org/10.1017/S0022112075001814.

Lazeroms, W. M., G. Svensson, E. Bazile, G. Brethouwer, S. Wallin, and A. V. Johansson, 2016: Study of transitions in the atmospheric boundary layer using explicit algebraic turbulence models. *Bound.-Layer Meteor.*, **161**, 19–47, https://doi.org/10.1007/s10546-016-0194-1.

Ludwig, F. L., F. K. Chow, and R. L. Street, 2009: Effect of turbulence models and spatial resolution on resolved velocity structure and momentum fluxes in large-eddy simulations of neutral boundary layer flow. *J. Appl. Meteor. Climatol.*, **48**, 1161–1180, https://doi.org/10.1175/2008JAMC2021.1.

Lumley, J. L., 1979: Computational modeling of turbulent flows. *Adv. Appl. Mech.*, **18**, 123–176, https://doi.org/10.1016/S0065-2156(08)70266-7.

Marstorp, L., G. Brethouwer, O. Grundestam, and A. V. Johansson, 2009: Explicit algebraic subgrid stress models with application to rotating channel flow. *J. Fluid Mech.*, **639**, 403–432, https://doi.org/10.1017/S0022112009991054.

Mellor, G. L., and T. Yamada, 1982: Development of a turbulence closure model for geophysical fluid problems. *Rev. Geophys.*, **20**, 851–875, https://doi.org/10.1029/RG020i004p00851.

Moeng, C.-H., 1984: A large-eddy-simulation model for the study of planetary boundary-layer turbulence. *J. Atmos. Sci.*, **41**, 2052–2062, https://doi.org/10.1175/1520-0469(1984)041<2052:ALESMF>2.0.CO;2.

Moin, P., K. Squires, W. Cabot, and S. Lee, 1991: A dynamic subgrid-scale model for compressible turbulence and scalar transport. *Phys. Fluids*, **3**, 2746–2757, https://doi.org/10.1063/1.858164.

Morrison, H., J. A. Curry, and V. I. Khvorostyanov, 2005: A new double-moment microphysics parameterization for application in cloud and climate models. Part I: Description. *J. Atmos. Sci.*, **62**, 1665–1677, https://doi.org/10.1175/JAS3446.1.

Muller, C. J., and I. M. Held, 2012: Detailed investigation of the self-aggregation of convection in cloud-resolving simulations. *J. Atmos. Sci.*, **69**, 2551–2565, https://doi.org/10.1175/JAS-D-11-0257.1.

Nakanishi, M., and H. Niino, 2009: Development of an improved turbulence closure model for the atmospheric boundary layer. *J. Meteor. Soc. Japan*, **87**, 895–912, https://doi.org/10.2151/jmsj.87.895.

Pope, S. B., 2000: Return-to-isotropy models. *Turbulent Flows*, Cambridge University Press, 392–404.

Prein, A. F., and Coauthors, 2015: A review on regional convection-permitting climate modeling: Demonstrations, prospects, and challenges. *Rev. Geophys.*, **53**, 323–361, https://doi.org/10.1002/2014RG000475.

Press, W. H., S. A. Teukolsky, W. T. Vetterling, and B. P. Flannery, 1992: *Numerical Recipes in Fortran 77*. 2nd ed. Cambridge University Press, 993 pp.

Pressel, K. G., S. Mishra, T. Schneider, C. M. Kaul, and Z. Tan, 2017: Numerics and subgrid-scale modeling in large eddy simulations of stratocumulus clouds. *J. Adv. Model. Earth Syst.*, **9**, 1342–1365, https://doi.org/10.1002/2016MS000778.

Ramachandran, S., and J. C. Wyngaard, 2011: Subfilter-scale modelling using transport equations: Large-eddy simulation of the moderately convective atmospheric boundary layer. *Bound.-Layer Meteor.*, **139**, 1–35, https://doi.org/10.1007/s10546-010-9571-3.

Rodi, W., 1976: A new algebraic relation for calculating the Reynolds stresses. *Z. Angew. Math. Mech.*, **56**, 219–221.

Ruelle, D., 2009: A review of linear response theory for general differentiable dynamical systems. *Nonlinearity*, **22**, 855, https://doi.org/10.1088/0951-7715/22/4/009.

Shabbir, A., and T. Shih, 1992: Critical assessment of Reynolds stress turbulence models using homogeneous flows. NASA Tech. Memo. 105954, ICOMP-92-24, CMOTT-92-12, 32 pp., https://ntrs.nasa.gov/archive/nasa/casi.ntrs.nasa.gov/19930007514.pdf.

Shi, X., H. L. Hagen, F. K. Chow, G. H. Bryan, and R. L. Street, 2018: Large-eddy simulation of the stratocumulus-capped boundary layer with explicit filtering and reconstruction turbulence modeling. *J. Atmos. Sci.*, **75**, 611–637, https://doi.org/10.1175/JAS-D-17-0162.1.

——, F. K. Chow, R. L. Street, and G. H. Bryan, 2019: Evaluation of some LES-type turbulence parameterizations for simulating

deep convection at kilometer-scale resolution. *J. Adv. Model. Earth Syst.*, **11**, https://doi.org/10.1029/2018MS001446.

Skamarock, W. C., and Coauthors, 2008: A description of the Advanced Research WRF version 3. NCAR Tech. Note NCAR/TN-475+STR, 113 pp., https://doi.org/10.5065/D68S4MVH.

Smagorinsky, J., 1963: General circulation experiments with the primitive equations: I. The basic experiment. *Mon. Wea. Rev.*, **91**, 99–164, https://doi.org/10.1175/1520-0493(1963)091<0099:GCEWTP>2.3.CO;2.

Stevens, B., and Coauthors, 2003: On entrainment rates in nocturnal marine stratocumulus. *Quart. J. Roy. Meteor. Soc.*, **129**, 3469–3493, https://doi.org/10.1256/qj.02.202.

——, and Coauthors, 2005: Evaluation of large-eddy simulations via observations of nocturnal marine stratocumulus. *Mon. Wea. Rev.*, **133**, 1443–1462, https://doi.org/10.1175/MWR2930.1.

Sullivan, P. P., T. W. Horst, D. H. Lenschow, C.-H. Moeng, and J. C. Weil, 2003: Structure of subfilter-scale fluxes in the atmospheric surface layer with application to large-eddy simulation modelling. *J. Fluid Mech.*, **482**, 101–139, https://doi.org/10.1017/S0022112003004099.

Tan, Z., C. M. Kaul, K. G. Pressel, Y. Cohen, T. Schneider, and J. Teixeira, 2018: An extended eddy-diffusivity mass-flux scheme for unified representation of subgrid-scale turbulence and convection. *J. Adv. Model. Earth Syst.*, **10**, 770–800, https://doi.org/10.1002/2017MS001162.

Tompkins, A. M., and A. G. Semie, 2017: Organization of tropical convection in low vertical wind shears: Role of updraft entrainment. *J. Adv. Model. Earth Syst.*, **9**, 1046–1068, https://doi.org/10.1002/2016MS000802.

Verrelle, A., D. Ricard, and C. Lac, 2017: Evaluation and improvement of turbulence parameterization inside deep convective clouds at kilometer-scale resolution. *Mon. Wea. Rev.*, **145**, 3947–3967, https://doi.org/10.1175/MWR-D-16-0404.1.

Wyngaard, J. C., 2004: Toward numerical modeling in the ''terra incognita.'' *J. Atmos. Sci.*, **61**, 1816–1826, https://doi.org/10.1175/1520-0469(2004)061<1816:TNMITT>2.0.CO;2.

Zelinka, M. D., S. A. Klein, K. E. Taylor, T. Andrews, M. J. Webb, J. M. Gregory, and P. M. Forster, 2013: Contributions of different cloud types to feedbacks and rapid adjustments in CMIP5. *J. Climate*, **26**, 5007–5027, https://doi.org/10.1175/JCLI-D-12-00555.1.

Zhou, B., and F. K. Chow, 2011: Large-eddy simulation of the stable boundary layer with explicit filtering and reconstruction turbulence modeling. *J. Atmos. Sci.*, **68**, 2142–2155, https://doi.org/10.1175/2011JAS3693.1.

——, and ——, 2014: Nested large-eddy simulations of the intermittently turbulent stable atmospheric boundary layer over real terrain. *J. Atmos. Sci.*, **71**, 1021–1039, https://doi.org/10.1175/JAS-D-13-0168.1.

Zilitinkevich, S. S., T. Elperin, N. Kleeorin, and I. Rogachevskii, 2007: Energy- and flux-budget (EFB) turbulence closure model for stably stratified flows. Part I: Steady-state, homogeneous regimes. *Bound.-Layer Meteor.*, **125**, 167–191, https://doi.org/10.1007/s10546-007-9189-2.